Epilepsy-related cytoarchitectonic abnormalities along white matter pathways

G. Russell Glenn BSc, BA[1-3], Jens H. Jensen PhD[1,2], Joseph A. Helpern PhD[1-3], Maria V Spampinato MD[2], Ruben Kuzniecky MD[4], Simon S Keller PhD[5,6], Leonardo Bonilha MD PhD[7]

1. Center for Biomedical Imaging, Medical University of South Carolina, Charleston, SC, USA
2. Department of Radiology and Radiological Science, Medical University of South Carolina, Charleston, SC, USA
3. Department of Neurosciences, Medical University of South Carolina, Charleston, SC, USA
4. Department of Neurology, New York University, New York, New York, USA
5. Department of Molecular and Clinical Pharmacology, Institute of Translational Medicine, University of Liverpool, Liverpool, UK
6. Department of Clinical Neuroscience, Institute of Psychiatry, King's College London, London, UK
7. Department of Neurology, Medical University of South Carolina, Charleston, SC, USA

Running title: Abnormalities along white matter pathways in epilepsy.

Manuscript word count: 3,499
Abstract word count: 247
Number of references: 39
Number of figures: 4
Number of tables: 2

Address correspondence to:

Leonardo Bonilha MD PhD
Associate Professor
Comprehensive Epilepsy Center
Department of Neurology
Medical University of South Carolina
96 Jonathan Lucas St, Suite 301
Charleston, SC. Zip code - 29425

Phone: 843 792 9590
email: bonilha@musc.edu

ABSTRACT

OBJECTIVE: Temporal lobe epilepsy (TLE) is one of the most common forms of epilepsy. Unfortunately, the clinical outcomes of TLE cannot be determined based only on current diagnostic modalities. A better understanding of white matter (WM) connectivity changes in TLE may aid the identification of network abnormalities associated with TLE and the phenotypic characterization of the disease.

METHODS: We implemented a novel approach for characterizing microstructural changes along WM pathways using diffusional kurtosis imaging (DKI). Along-the-tract measures were compared for 32 subjects with left TLE and 36 age- and gender-matched controls along the left and right fimbria-fornix (FF), parahippocampal WM bundle (PWMB), arcuate fasciculus (AF), inferior longitudinal fasciculus (ILF), uncinate fasciculus, and cingulum bundle (CB). Limbic pathways were investigated in relation to seizure burden and control with anti-epileptic drugs.

RESULTS: By evaluating measures along each tract, it was possible to identify abnormalities localized to specific tract sub-regions. Compared with healthy controls, subjects with TLE demonstrated pathological changes in circumscribed regions of the FF, PWMB, UF, AF and ILF. Several of these abnormalities were detected only by kurtosis-based and not by diffusivity-based measures. Structural WM changes correlated with seizure burden in the bilateral PWMB and cingulum.

CONCLUSIONS: DKI improves the characterization of network abnormalities associated with TLE by revealing connectivity abnormalities that are not disclosed by other modalities. Since TLE is a neuronal network disorder, DKI may be well suited to fully assess structural network abnormalities related to epilepsy and thus serve as a tool for phenotypic characterization of epilepsy.

INTRODUCTION

Temporal lobe epilepsy (TLE) is the most common form of medically intractable focal epilepsy and is frequently associated with hippocampal sclerosis (HS) (1). Despite that hippocampal pathology is generally considered the primary seizure generator and principal node in a temporal epileptiform network in TLE (2), there is a sizeable literature indicating that structural abnormalities extend beyond the medial temporal lobe. Many studies have reported gray matter atrophy, white matter (WM) loss, and gliosis affecting extra-hippocampal and extra-temporal regions (3-6). Crucially, the distribution of tissue damage in TLE is not random, but follows an anatomical and functional pattern whereby the most affected regions are those directly or indirectly associated with the medial temporal lobe and the limbic system (7-9). This regular distribution of damage implies that a limited number of common pathophysiological mechanisms are responsible for brain injury in TLE. In particular, gray matter loss may be caused by cellular excitoxicity along the limbic path of seizure spread, or by deafferentation injury from loss of neural connectivity (10).

However, the full extent of microstructural brain damage in TLE is still incompletely understood, and most patients with TLE demonstrate some degree of extra-hippocampal abnormality (11). Importantly, seizure control after pharmacological and surgical intervention can vary significantly among patients with TLE, and there are clearly distinct phenotypes of TLE when it comes to treatment responsiveness. For this reason, it is fundamentally important to accurately assess *in vivo* patterns of brain injury

in TLE, with special emphasis to cytoarchitectonic features of tissue damage and their anatomical distribution.

Previous studies have investigated alterations in WM pathways in TLE using diffusion tensor tractography (12-14). However, these studies predominantly utilize whole-tract analyses, which are limited as pathological changes may be concentrated in anatomically specific regions and whole-tract analyses may obstruct the detection of focal pathology. Moreover, diffusion tensor imaging (DTI) is incapable of detecting multiple, intra-voxel fiber bundle orientations in complex neurological tissue, which limits its potential for tractography (15,16). Diffusional kurtosis imaging (DKI) extends conventional DTI by estimating both the diffusion and kurtosis tensors to quantify restricted, non-Gaussian diffusion that occurs in biological tissues (17,18). Accordingly, DKI has demonstrated improved sensitivity for detecting neuropathology in a variety of conditions including epilepsy (19-22), stroke (23-26), Alzheimer's disease (27-29), and numerous others. More recently, the advantages of DKI have been leveraged to provide more comprehensive assessment of diffusion in complex neural environments, including the characterization of diffusion anisotropy beyond the conventional fractional anisotropy (FA) (30) and computation of DKI-based WM tractography, enabling the resolution of multiple intra-voxel fiber bundles (16,31). These advantages are improved by utilizing DKI in conjunction with automated fiber quantification (AFQ) (32), for characterization of tissue microstructure along WM pathways, by incorporating a more comprehensive and potentially more sensitive collection of parameters for detecting disease-related pathology than does DTI. Thus, DKI is remarkably synergistic with AFQ,

and the combination of the two form a particularly effective imaging method for detecting pathological WM changes.

In this present study, we applied a novel neuroimaging approach combining the strengths of DKI and AFQ for the non-invasive characterization of pathological WM changes in TLE. We hypothesize that cytoarchitectural abnormalities follow a crescendo gradient towards the temporal lobe with pathological effects concentrated in particular WM regions, revealing patterns of neuroarchitectural pathology associated with TLE potentially underlying distinct phenotypical subtypes.

METHODS

Subjects

This study was approved by the Institutional Review Board at the Medical University of South Carolina (MUSC). We evaluated data from 32 consecutive subjects with left TLE who were followed at the Comprehensive Epilepsy Center at MUSC. All subjects were diagnosed with left TLE in concordance with the diagnostic criteria proposed by the International League Against Epilepsy (ILAE), including a comprehensive medical history, a full neurological evaluation, and epileptiform discharges on interictal EEG, with the majority of subjects demonstrating neuroradiological evidence of HS (33). The mean (± std) age of all subjects was 44.8 (± 16.7) years, and included 10 males and 22 females. A control group of 36 age and gender matched healthy individuals with no history of neurological problems was also

recruited from the local community. Control subjects had a mean (± std) age of 40.4 (± 11.6) years, including 12 males and 24 females. Clinical and demographic information for the subjects with TLE included in this study are further described in the table provided in the online supplemental material. The subjects included in this study are also described in a previous study from our group using voxel-based methods without tractography (22).

Our cohort contained subjects with varying disease severity including subjects with recently diagnosed TLE and subjects whose seizures were well controlled with anti-epileptic drugs (AEDs). Thus subjects in this cohort were not all surgical candidates. Subjects well controlled on AEDs were identified by having one or fewer seizures per six months (n = 13), and subjects not well controlled on AEDs were identified by having more than one seizure per six months (n = 19).

Image Acquisition and Analysis

Image acquisition was performed on a 3 Tesla Magnetom Verio MRI scanner (Siemens Medical, Erlangen, Germany) and included a DKI data set and T1-weighted images. DKI analysis included characterization of mean diffusivity (MD) and FA from the diffusion tensor and corresponding mean kurtosis (MK) and kurtosis fractional anisotropy (KFA) (30). DKI-derived tractography (16,31) was performed using diffusional kurtosis estimator software (https://www.nitrc.org/projects/dke/). DKI was incorporated into the AFQ image processing pipeline (https://github.com/jyeatman/AFQ) using fully automated in-house scripts, which included along-the-tract characterization

of the fimbria-fornix (FF), parahippocampal white matter bundle (PWMB), arcuate fasciculus (AF), inferior longitudinal fasciculus (ILF), cingulum bundle (CB) and uncinate fasciculus (UF).

The effects of seizure burden and seizure control with AEDs were tested in the PWMB and CB, as these limbic pathways are crucial for the progression of disease (12), neuropsychological manifestations of TLE (14), and differentiation of TLE subtypes by treatment response including surgical outcomes (34,35) and pharmacoresistance (36). Seizure burdfen was defined as equal to $\log_{10}(frequency \times duration)$, with the logarithm being applied to accommodate subjects with very high seizure frequency, and the effects were assessed using Pearson's product-moment correlation coefficient.

A summary of the image analysis steps for a single subject is given in Figure 1, and a detailed description of our image acquisition protocol and image analysis steps is given in the online supplemental material.

Statistical Analysis

Individual tract profiles were averaged over 5 regions of interest (ROIs), and a two sample t-test was performed to determine the significance of group-wise differences. Significance levels were corrected for multiple comparisons using the false discovery rate (FDR) procedure (37). For correlations with seizure burden, statistical significance was corrected for multiple comparisons with FDR, and the effects of pharmacoresistance were tested using the well-controlled and not well-controlled groups using a two sample t-test. Cohen's d parameter was used to quantify the effect size. The ROIs used in this study are illustrated in Figure 2.

RESULTS

Group-wise tract profiles for all fiber groups are shown in Figure 3. The tract profiles demonstrate similar along-the-tract variation of the diffusion metrics between subjects and controls and between the ipsilateral and contralateral hemispheres. Importantly, these results demonstrate that epilepsy-related abnormalities can be restricted to specific regions of each tract, which would be undetected by methods that group all data from one tract into a single value. The results in Figure 3 are tabulated in the online supplemental material.

In general, MD is higher in subjects with TLE relative to controls in all ROIs and all fiber groups with the exception of one ipsilateral ROI (ROI 3 in the UF) and eight contralateral ROIs (ROI 1 and 5 in the FF, ROI 1 in the AF, ROI 2 and 3 in the UF, and ROIs 3-5 in the right ILF), although the observed changes were not found to be statistically significant. FA tended to be lower in subjects with TLE relative to controls, with statisitically significant reductions being found in ROIs 4 and 5 of the ipsilateral AF.

MK demonstrated significant reduction in the ipsilateral FF, PWMB, and UF in multiple ROIs. In the ipsilateral FF and UF, this reduction was more pronounced with increasing ROI number (further anteriorly within the temporal lobe). MK showed statistically significant reductions in all ROIs in the bilateral AF and ILF, except for ROI 1 in the contralateral AF and ROI 3 in the contralateral ILF, with the ipsilateral side tending to demonstrate a stronger effect size.

The location and relative significance of the observed differences are illustrated in the section-wise t-score plots in Figure 4. Qualitatively, the abnormal t-scores demonstrated a crescendo effect increasing in significance into the temporal lobe. Similar to the tract profiles, the section-wise t-score plots demonstrated a slight, but general increase in MD and decrease in FA in subjects relative to controls. With MK, the changes can be seen bilaterally, with the effect being the largest within the ipsilateral temporal lobe.

Correlations with seizure burden are illustrated in Table 1. Significant correlations were found in the PWMB and CB with MD demonstrating significant correlations on the ipsilateral hemisphere and MK and KFA demonstrating bilateral limbic effects. In the ipsilateral PWMB, significant correlations were found for MD, MK, and KFA in ROI 3, with the correlations extending further along the tract anteriorly and posteriorly with MD and KFA. In the ipsilateral CB, significant correlations were found in ROI 5 for MD, ROIs 2-5 for MK, and all ROIs for KFA. On the contralateral side, significant correlations with MK were found in ROI 3 of the PWMB and ROIs 2-5 of the CB, and with KFA in ROI 3 and 4 of the PWMB and ROI 5 of the CB.

Comparisons between AED responsive and unresponsive groups are illustrated in Table 2. Uncorrected p-values less than 0.05 were found in comparing subjects well-controlled with AEDs with those poorly controlled for the ipsilateral PWMB in ROI 3 in MD and ROIs 3-4 in KFA and for the ipsilateral CB in ROI 5 in MD and all ROIs with the anisotropy parameters, FA and KFA. Uncorrected p-values less than 0.05 were also found for the contralateral CB in MK in ROI 2 and KFA in ROI 5. While none of these

attained statistical significance following FDR correction, they may be indicative of trends that would warrant further investigation with a larger sample size. For example, the not well-controlled group demonstrated a 21% reduction in KFA in ROI 2 of the ipsilateral CB compared to the well-controlled group with a Cohen's d parameter of -1.262, suggesting a potentially large effect.

DISCUSSION

In this study, we employed a novel neuroimaging technique that combines DKI and AFQ for the in vivo characterization of cytoarchitectronic abnormalities in TLE along WM pathways which are physiologically relevant for TLE. In accordance with the previous literature, we detected pathological changes in several extra-hippocampal and extra-temporal WM tracts in subjects with TLE. Moreover, the important novel findings of this study pertain to the superior sensitivity of DKI-based tractography to identify and localize intra-pathway structural connectivity abnormalities in TLE. These observations complement our initial reports of increased sensitivity of DKI in scalar diffusion voxel-based maps of subjects with epilepsy (22). This is the first study to use DKI-based tractography combined with AFQ, demonstrating how DKI tractography can overcome limitations imposed by fiber crossing and unveil epilepsy related abnormalities. Our data indicate that group-wise reductions in MK are observed in regionally specific areas of the ipsilateral FF, UF, and PWMB, as well as more diffuse bilateral abnormalities in the ILF and AF (Figure 3). We also report significant effects of seizure burden on MD, MK, and KFA of ipsilateral limbic pathways. MK and KFA indicated additional correlations

with seizure burden in contralateral pathways (Table 1). The overall salience of these findings hinges on the technical innovations of these new forms of tractography and the critical need to better define phenotypic characterizations of subjects with epilepsy.

Technical Innovations

This is the first study to combine DKI and AFQ for the fully automated detection of cytoarchitectonic alterations along WM fiber pathways, which may be a particularly sensitive method for assessing WM tissue microstructure. With scalar, voxel-based data, it is not always clear which pathways are compromised. For example, an abnormal voxel in an ROI corresponding to the ILF may be related to transverse fibers in the same region. By defining which specific tracts are abnormal, one can develop a more detailed understanding of the distribution of cytoarchitectonic abnormalities. The methodological benefits of these approaches are further enhanced when augmented with along the tract measures, which not only identify the structurally compromised tracts, but additionally have the capability to localize specific abnormalities within the long axis of a tract. Moreover, the tract cores analyzed can preserve a significant amount of inter-subject anatomical tract variability while still enabling group-wise comparisons, which can help avoid normalization errors that complicate conventional voxel-wise techniques. This is further improved by utilizing DKI, which characterizes higher-order diffusion dynamics compared to DTI and can thus describe more complex diffusion profiles. Consequently, DKI enables the detection of crossing WM fiber bundles for diffusion tractography and provides a more comprehensive collection of

quantitative parameters, which may enhance the detection of disease-related abnormalities. Thus, the combination of DKI and AFQ creates an effective tool for characterizing WM pathways, enabling further insights into patterns of neuroarchitectural pathology that occur in numerous neurological and psychiatric disorders.

Towards a phenotypic microstructural connectivity characterization of TLE

Increasingly, advanced neuroimaging techniques have demonstrated both localized and networked cytoarchitectonic abnormalities in TLE with limbic alterations potentially underlying various clinicopathological features of the disorder, including the pathological mechanisms that lead to medically intractable TLE (12), neuropsychological impairments (14), AED response (36), and surgical outcomes (34,35). In the present study, we recruited a cohort of 32 consecutive subjects diagnosed with left TLE, which was comprised of subjects with various disease severities. DKI in combination with AFQ detected pathological WM alterations consistent with our understanding of TLE as a network disease having tissue abnormalities concentrated in the temporal lobe of the brain. Moreover, statistical trends were observed in limbic structures between subjects whose seizures were well controled with AEDs and those who had worse AED control (Table 2), which could be an important clinical prognosticator. Interestingly, KFA in the ipsilateral PWMB and CB correlated with seizure burden, and we observed trends for differences in tract characteristics between subjects who had well-controlled seizures and those who did

not, despite no detectible group-wise differences in this region with normal controls. A similar trend was seen between subjects who had well-controlled seizures with AEDs and those who did not in FA in the ipsilateral CB. A possible explanation for this is that distinct mechanisms may underlie AED response compared to pharmacoresistance, with AED responders having higher than normal diffusion anisotropy and subjects whose seizures were not well controlled having lower than normal diffusion anisotropy in these limbic structures. This also supports the need for the improved sensitivity in detecting patterns of neuroarchitectural alterations in TLE afforded by DKI. Moreover, DKI detected contralateral changes in MK that were not apparent in analysis of the conventional diffusivity-based parameters of MD and FA.

This study also extends the work of Concha et al. (38), where along-the-tract measures were assessed in the ILF, AF, and UF using a manual segmentation routine with DTI in subjects with medically intractable TLE. In that work, it was argued that the changes in diffusion metrics could reflect astrogliosis and microstructural alterations related to the occurrence of seizures with potential effects of postictal vasogenic edema. In the present study, the reduction in MK reflects a net loss in the complexity of microstructural tissue compartmentalization, which is also consistent with subtle pathological denervation. By including a more comprehensive assessment of along-the-tract diffusion abnormalities, the proposed technique may provide an important step towards a better understanding of the neuroarchitectural alterations that occur in TLE, as well as the development of fully automated imaging biomarkers for the separation of TLE subtypes based on clinically important distinctions.

Limitations

By focusing this study on tract profiles within the AFQ identified tract cores and using only a subset of the possible DKI-derived diffusion metrics, we have substantially restricted the scope of our analysis. This is a potential limitation of this study, as there may be important disease-related differences missed outside of the tract cores. Moreover, the quantitative parameters employed in this study depict physical properties of water diffusion which may be differentially influenced by multiple, distinct factors (15). To address this limitation DKI-based WM modeling techniques can be applied, which may improve the specificity of the observed changes (39). The subject cohort included in this study was comprised of individuals with left-sided TLE, as left- and right-sided TLE may have intrinsically different pathological effects on temporal lobe structures (40). Thus we were not able to assess the effects of right sided disease. In addition, this study was comprised of individuals with variying disease severity, including recently diagnosed and chronic TLE as well as individuals whose seizures were well-controlled and not well-controlled with AEDs. Well-controlled and intractable TLE may represent distinct pathological mechanisms; so by including both groups, sensitivity may be lost in characterizing regionally specific distinctions. Nevertheless, combining DKI with AFQ revealed distinct patterns of cytoarchitectronic abnormalities, which highlights the sensitivity as well as the potential applicability of the proposed techique.

Conclusion

There are measurable differences in WM tissue that are not routinely considered in the clinical assessment of subjects with unilateral TLE. We have described a diffusion MRI-based image analysis technique that, by combining the strengths of DKI and AFQ, can quantify cytoarchitectonic abnormalities in specific, WM fiber pathways. The proposed technique is shown to detect group-wise pathological changes, with the largest effect sizes lateralizing to the ipsilateral temporal lobe and extending along the tracts from the ipsilateral temporal lobe and including the contralateral side of the brain. Microstructural changes are also found to correlate with seizure burden in specific limbic pathways and trends are found towards detecting differences between subjects with well-controlled and not well-controlled TLE. Combining DKI and AFQ may be a particularly effective neuroimaging technique for detecting microstructural alterations along physiologically relevant WM pathways that could provide further insights into the variable clinical course of TLE, as well as a wide array of other neuropsychological conditions affecting the structural organization of the human brain.

FUNDING

This work was supported in part by the National Institutes of Health grant T32GM008716 (to P. Halushka) and by the Litwin Foundation (to J.A.H).

REFERENCES

1. Babb TL, Brown WJ. Pathological findings in epilepsy. In: Engel JJ, ed. Surgical Treatment of the Epilepsies. New York: Raven; 1987: 511–40.
2. Haneef Z, Lenartowicz A, Yeh HJ, Levin HS, Engel J Jr, Stern JM. Functional connectivity of hippocampal networks in temporal lobe epilepsy. Epilepsia. 2014;55:137-45.
3. Gross DW, Concha L, Beaulieu C. Extratemporal white matter abnormalities in mesial temporal lobe epilepsy demonstrated with diffusion tensor imaging. Epilepsia. 2006 Aug;47(8):1360-3.
4. Keller SS, Roberts N. Voxel-based morphometry of temporal lobe epilepsy: an introduction and review of the literature. Epilepsia. 2008;49:741–757.
5. Concha L, Beaulieu C, Collins DL, et al. White-matter diffusion abnormalities in temporal-lobe epilepsy with and without mesial temporal sclerosis. J Neurol Neurosurg Psychiatry.2009;80:312-319.
6. Bernhardt BC, Hong S, Bernasconi A, Bernasconi N. Imaging structural and functional brain networks in temporal lobe epilepsy. Front Hum Neurosci. 2013;7:624.
7. Coan AC, Appenzeller S, Bonilha L, Li LM, Cendes F. Seizure frequency and lateralization affect progression of atrophy in temporal lobe epilepsy. Neurology. 2009;73:834-42.
8. Bonilha L, Kobayashi E, Rorden C, Cendes F, Li LM. Medial temporal lobe atrophy in patients with refractory temporal lobe epilepsy. J Neurol Neurosurg Psychiatry 2003;74:1627–1630.

9. McMillan AB, Hermann BP, Johnson SC, Hansen RR, Seidenberg M, Meyerand ME. Voxel-based morphometry of unilateral temporal lobe epilepsy reveals abnormalities in cerebral white matter. Neuroimage 2004;23:167–174.
10. Bonilha L, Edwards JC, Kinsman SL, Morgan PS, Fridriksson J, Rorden C, Rumboldt Z, Roberts DR, Eckert MA, Halford JJ. Extrahippocampal gray matter loss and hippocampal deafferentation in patients with temporal lobe epilepsy. Epilepsia. 2010;51:519-28.
11. Bonilha L, Elm JJ, Edwards JC, Morgan PS, Hicks C, Lozar C, Rumboldt Z, Roberts DR, Rorden C, Eckert MA. How common is brain atrophy in patients with medial temporal lobe epilepsy? Epilepsia. 2010;51:1774-9.
12. Concha L, Beaulieu C, Gross DW Bilateral limbic diffusion abnormalities in unilateral temporal lobe epilepsy. Ann Neurol. 2005;57:188-96.
13. Yogarajah M, Duncan JS. Diffusion-based magnetic resonance imaging and tractography in epilepsy. Epilepsia 2008;49:189-200.
14. McDonald CR, Ahmadi ME, Hagler DJ, Tecoma ES, Iragui VJ, Gharapetian L, Dale AM, Halgren E. Diffusion tensor imaging correlates of memory and language impairments in temporal lobe epilepsy. Neurology. 2008;71:1869-76.
15. Jones DK, Knösche TR, Turner R. White matter integrity, fiber count, and other fallacies: the do's and don'ts of diffusion MRI. Neuroimage. 2013;73:239-54.
16. Jensen JH, Helpern JA, Tabesh A (2014): Leading non-Gaussian corrections for diffusion orientation distribution functions. NMR Biomed. 27:202-11.

17. Jensen JH, Helpern JA, Ramani A, Lu H, Kaczynski K. Diffusional kurtosis imaging: the quantification of non-Gaussian water diffusion by means of magnetic resonance imaging. Magn Reson Med. 2005;53:1432-40.
18. Jensen JH, Helpern JA. MRI quantification of non-Gaussian water diffusion by kurtosis analysis. NMR Biomed. 2010;23:698-710.
19. Gao Y, Zhang Y, Wong CS, Wu PM, Zhang Z, Gao J, Qiu D, Huang B. Diffusion abnormalities in temporal lobes of children with temporal lobe epilepsy: a preliminary diffusional kurtosis imaging study and comparison with diffusion tensor imaging. NMR Biomed. 2012;25:1369-77.
20. Gao J, Feng ST, Wu B, Gong N, Lu M, Wu PM, Wang H, He X, Huang B. Microstructural brain abnormalities of children of idiopathic generalized epilepsy with generalized tonic-clonic seizure: a voxel-based diffusional kurtosis imaging study. J Magn Reson Imaging. 2015;41:1088-95.
21. Lee CY, Tabesh A, Benitez A, Helpern JA, Jensen JH, Bonilha L. Microstructural integrity of early- versus late-myelinating white matter tracts in medial temporal lobe epilepsy. Epilepsia. 2013;54:1801-9.
22. Bonilha L, Lee CY, Jensen JH, Tabesh A, Spampinato MV, Edwards JC, Breedlove J, Helpern JA. Altered microstructure in temporal lobe epilepsy: a diffusional kurtosis imaging study. AJNR Am J Neuroradiol. 2015;36:719-24.
23. Jensen JH, Falangola MF, Hu C, Tabesh A, Rapalino O, Lo C, Helpern JA. Preliminary observations of increased diffusional kurtosis in human brain following recent cerebral infarction. NMR Biomed. 2011;24:452-7.

24. Fung SH, Roccatagliata L, Gonzalez RG, Schaefer PW. MR diffusion imaging in ischemic stroke. Neuroimaging Clin N Am. 2011;21:345-77.
25. Hui ES, Fieremans E, Jensen JH, Tabesh A, Feng W, Bonilha L, Spampinato MV, Adams R, Helpern JA. Stroke assessment with diffusional kurtosis imaging. Stroke. 2012;43:2968-73.
26. Umesh Rudrapatna S, Wieloch T, Beirup K, Ruscher K, Mol W, Yanev P, Leemans A, van der Toorn A, Dijkhuizen RM. Can diffusion kurtosis imaging improve the sensitivity and specificity of detecting microstructural alterations in brain tissue chronically after experimental stroke? Comparisons with diffusion tensor imaging and histology. Neuroimage. 2014;97:363-73.
27. Falangola MF, Jensen JH, Tabesh A, Hu C, Deardorff RL, Babb JS, Ferris S, Helpern JA. Non-Gaussian diffusion MRI assessment of brain microstructure in mild cognitive impairment and Alzheimer's disease. Magn Reson Image. 2013; 31:840-6.
28. Benitez A, Fieremans E, Jensen JH, Falangola MF, Tabesh A, Ferris SH, Helpern JA. White matter tract integrity metrics reflect the vulnerability of late-myelinating tracts in Alzheimer's disease. Neuroimage Clin. 2013;9:64-71.
29. Fieremans E, Benitez A, Jensen JH, Falangola MF, Tabesh A, Deardorff RL, Spampinato MV, Babb JS, Novikov DS, Ferris SH, Helpern JA. Novel white matter tract integrity metrics sensitive to Alzheimer disease progression. Am J Neuroradiol. 2013;34:2105-12.

30. Glenn GR, Helpern JA, Tabesh A, Jensen JH (2015c): Quantitative assessment of diffusional kurtosis anisotropy. NMR Biomed. 28:448-59.
31. Glenn GR, Helpern JA, Tabesh A, Jensen JH. Optimization of white matter fiber tractography with diffusional kurtosis imaging. NMR Biomed. NMR Biomed. 2015;28:1245-56.
32. Yeatman JD, Dougherty RF, Myall NJ, Wandell BA, Feldman HM. Tract profiles of white matter properties: automating fiber-tract quantification. PLoS One. 2012;7:e49790.
33. Blümcke I, Thom M, Aronica E, Armstrong DD, Bartolomei F, Bernasconi A, Bernasconi N, Bien CG, Cendes F, Coras R, Cross JH, Jacques TS, Kahane P, Mathern GW, Miyata H, Moshé SL, Oz B, Özkara Ç, Perucca E, Sisodiya S, Wiebe S, Spreafico R. International consensus classification of hippocampal sclerosis in temporal lobe epilepsy: a Task Force report from the ILAE Commission on Diagnostic Methods. Epilepsia. 2013;54:1315-29.
34. Bonilha L, Yasuda CL, Rorden C, Li LM, Tedeschi H, de Oliveira E, Cendes F. Does resection of the medial temporal lobe improve the outcome of temporal lobe epilepsy surgery? Epilepsia. 2007;48:571-8.
35. Bonilha L, Martz GU, Glazier SS, Edwards JC. Subtypes of medial temporal lobe epilepsy: influence on temporal lobectomy outcomes? Epilepsia. 2012;53:1-6.

36. Bilevicius E, Yasuda CL, Silva MS, Guerreiro CA, Lopes-Cendes I, Cendes F. Antiepileptic drug response in temporal lobe epilepsy: a clinical and MRI morphometry study. Neurology. 2010;75:1695-701.
37. Benjamini, Yoav; Hochberg, Yosef. Controlling the false discovery rate: a practical and powerful approach to multiple testing. J R Stat Soc Series B. 1995;57:289–300.
38. Concha L, Kim H, Bernasconi A, Bernhardt BC, Bernasconi N. Spatial patterns of water diffusion along white matter tracts in temporal lobe epilepsy. Neurology. 2012;79:455-62.
39. Fieremans E, Jensen JH, Helpern JA. White matter characterization with diffusional kurtosis imaging. Neuroimage 2011;58:177–188.
40. Keller SS, Mackay CE, Barrick TR, Wieshmann UC, Howard MA, Roberts N. Voxel-based morphometric comparison of hippocampal and extrahippocampal abnormalities in patients with left and right hippocampal atrophy. Neuroimage. 2002;16:23-31.

FIGURE CAPTIONS

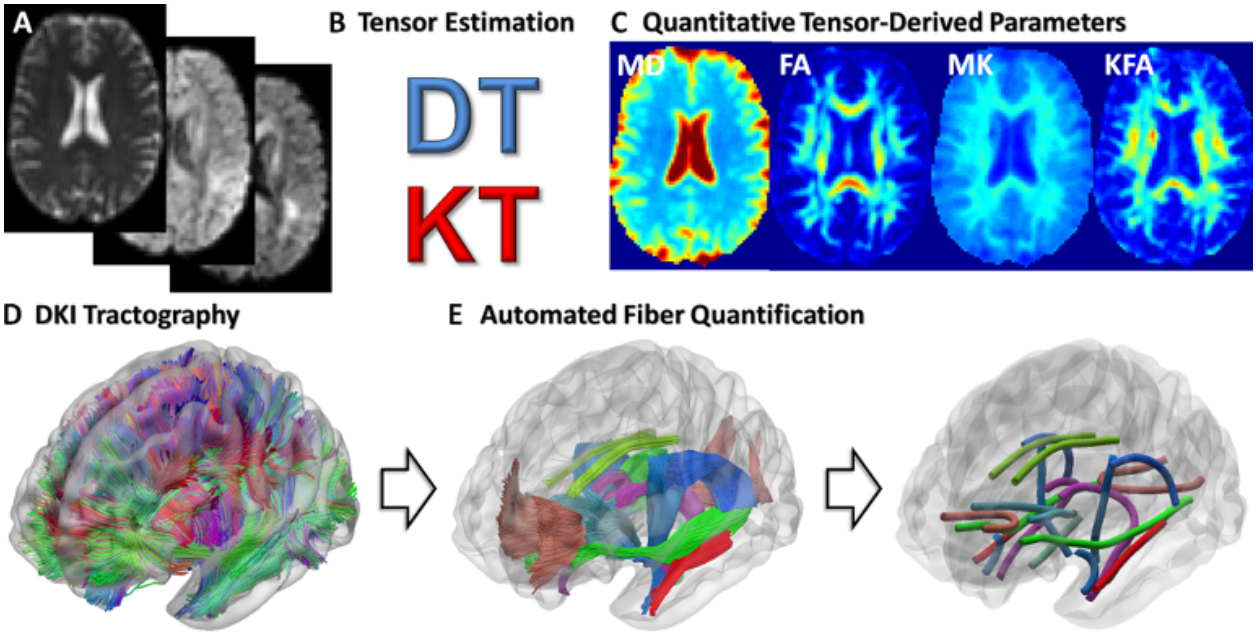

Figure 1. AFQ with DKI. (A) DKI uses multiple diffusion weighting b-values and diffusion encoding directions to characterize non-Gaussian diffusion which occurs in vivo. The images shown include an average b=0 image along with images with diffusion weightings of b = 1000 and b = 2000 s/mm^2 for a single diffusion-encoding direction. (B) Images in the DKI dataset are combined to estimate the diffusion tensor (DT) and kurtosis tensor (KT), which characterize the 3D intra-voxel diffusion dynamics based on physical properties of water diffusion. (C) The diffusion and kurtosis tensors are then analyzed to generate scalar, quantative parameter maps that can be used to characterize tissue microstructure. (D) The diffusion and kurtosis tensors are combined to perform DKI-based tractography, which can improve tractography relative to DTI by enabling the resolution of multiple intra-voxel fiber bundles in complex neural tissue. (E) AFQ performs a series of automated steps to segment fiber groups from standardized WM ROIs and then isolates each fiber group's tract core for analysis of the diffusion

parameters. Each subject generates tract profiles for each diffusion metric along each tract core, which can be compared to investigate individual and group-wise differences.

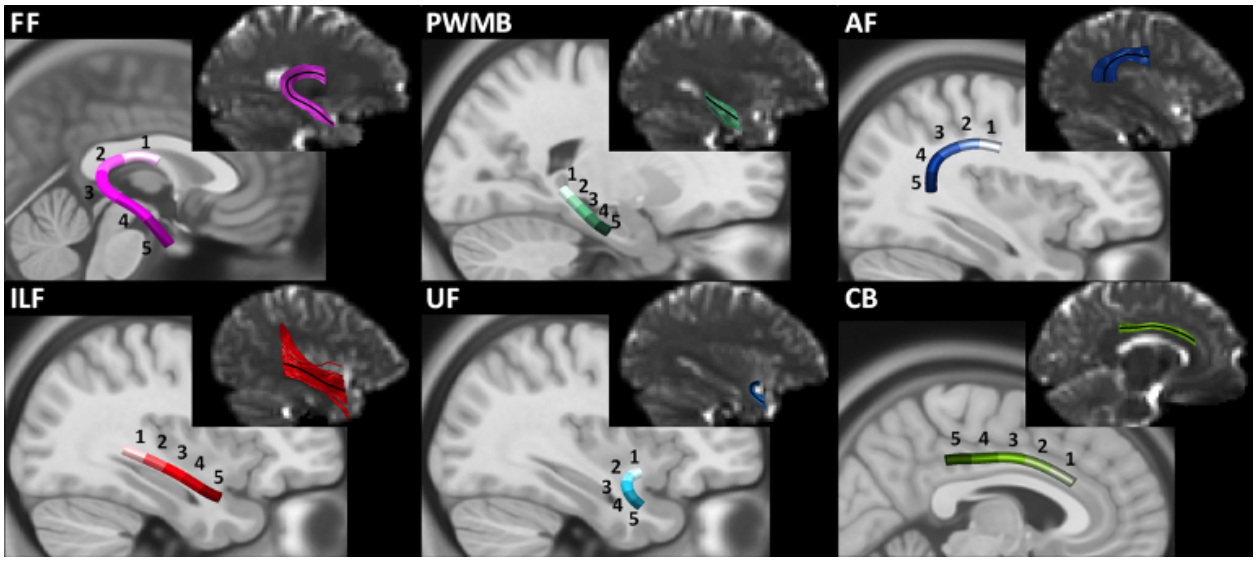

Figure 2. The location of WM ROIs is defined from the reconstructed fiber tracts. The insert for each fiber group in the upper right-hand corner illustrates WM tracts identified by AFQ and DKI for a single subject, overlaid on the corresponding b=0 image. The solid black line indicates the core of each tract used in generating the individual tract profiles. Tract cores identified for all subjects in this study are averaged and overlaid on an anatomical MRI template to illustrate the group-wise representation of each fiber group. Each fiber group is divided into 5 ROIs with increasing ROI numbers indicating regionally-specific locations in each tract. The ROIs in this figure correspond to the ROIs used in the tables included in this study.

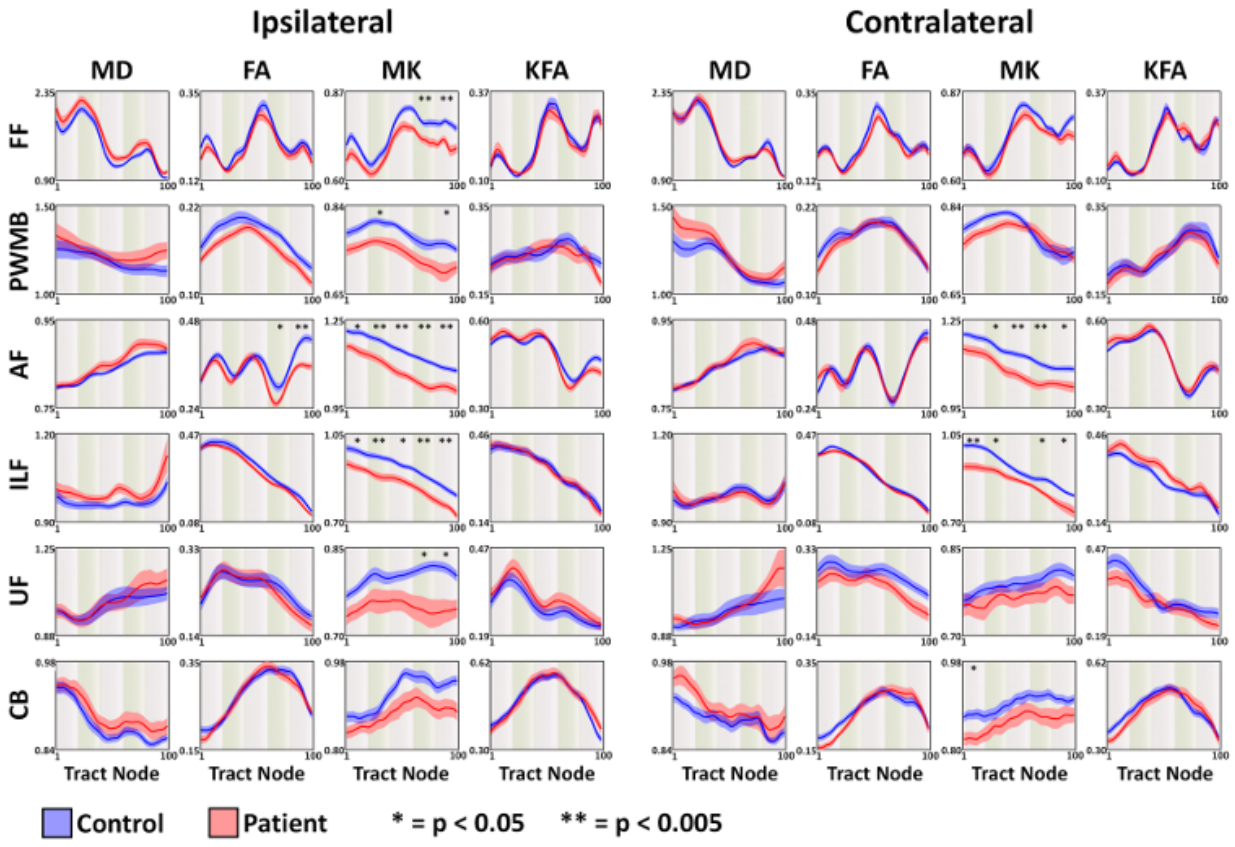

Figure 3. Mean tract profiles (± sem) for ipsilateral and contralateral fiber groups demonstrate regional group-wise differences in diffusion metrics between subjects and controls. Group-wise differences are tested over bins indicated by the green and purple bars and summary statistics for group-wise comparisons are given in the online supplemental material. Comparisons marked with an asterisk (*) have p-values < 0.05, and a double asterisk (**) indicates p-values < 0.005, after correction the significance level for multiple comparisons using FDR. The vertical bins correspond to the ROIs illustrated in Figure 2 with increasing ROI number corresponding to increasing Tract Section number. The MD is in units of $\mu m^2/ms$, while the remaining parameters are dimensionless.

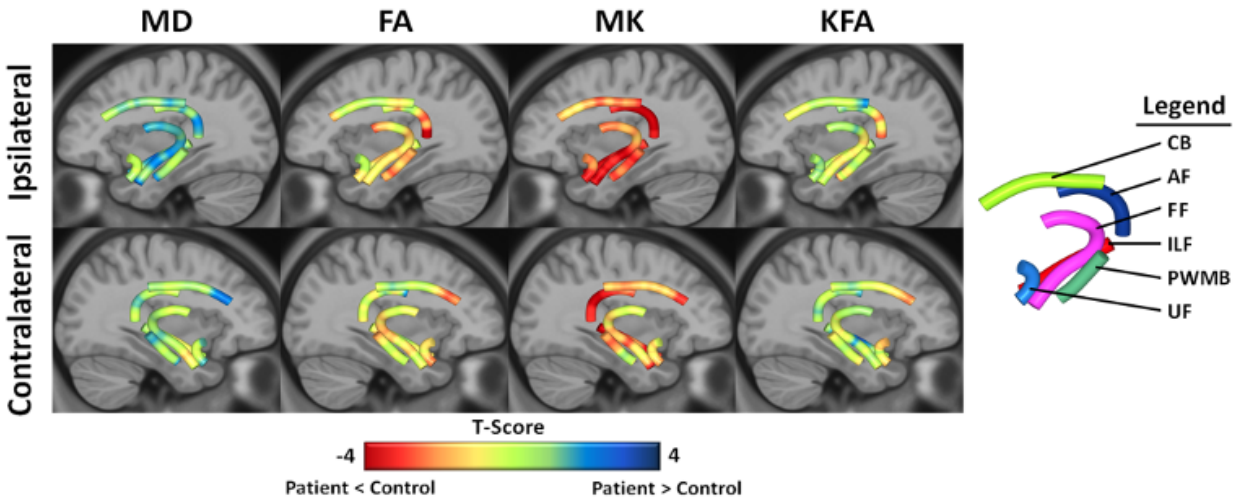

Figure 4. Section-wise t-score plots summarize the observed differences in the tract profiles. Section wise t-scores are calculated from the tract profiles illustrated in Figure 3. These are overlaid on a WM template at positions indicated by the average of the tract-cores for all participants included in this study. Section-wise t-scores provide a visual representation of where pathological changes occur, with dark red indicating greater group-wise reductions in the subject versus control groups and dark blue indicating greater group-wise increases in the subjects versus control group.

TABLES

Parahippocampal White Matter Bundle

Param	ROI	Correlation with Seizure Burden					
		Left			Right		
		Pearson's r	p-value		Pearson's r	p-value	
MD	1	0.272	0.196		0.310	0.150	
	2	**0.442**	**0.038**	*	0.279	0.197	
	3	**0.602**	**0.007**	*	0.342	0.129	
	4	**0.532**	**0.017**	*	0.386	0.083	
	5	**0.457**	**0.036**	*	0.277	0.197	
FA	1	-0.122	0.547		-0.089	0.665	
	2	-0.214	0.304		-0.166	0.430	
	3	-0.246	0.238		-0.285	0.192	
	4	-0.202	0.329		-0.130	0.542	
	5	0.138	0.502		-0.190	0.369	
MK	1	0.120	0.549		0.174	0.408	
	2	0.325	0.132		0.204	0.339	
	3	**0.484**	**0.027**	*	**0.436**	**0.050**	*
	4	0.397	0.070		0.396	0.076	
	5	0.233	0.262		0.329	0.142	
KFA	1	-0.258	0.212		-0.253	0.236	
	2	**-0.459**	**0.036**	*	-0.336	0.135	
	3	**-0.623**	**0.006**	*	**-0.465**	**0.035**	*
	4	**-0.564**	**0.009**	*	**-0.452**	**0.039**	*
	5	-0.306	0.148		-0.313	0.147	

Cingulum Bundle

Param	ROI	Correlation with Seizure Burden					
		Left			Right		
		Pearson's r	p-value		Pearson's r	p-value	
MD	1	0.336	0.126		0.099	0.622	
	2	0.314	0.140		0.187	0.364	
	3	0.316	0.138		0.176	0.390	
	4	**0.386**	**0.075**	*	0.261	0.209	
	5	**0.446**	**0.037**	*	0.331	0.132	
FA	1	-0.212	0.305		-0.060	0.765	
	2	-0.284	0.178		-0.003	0.986	
	3	-0.338	0.127		0.024	0.908	
	4	**-0.358**	**0.098**	*	-0.219	0.296	
	5	-0.303	0.150		-0.390	0.073	I
MK	1	0.415	0.054		0.394	0.071	
	2	**0.518**	**0.019**	*	**0.566**	**0.010**	*
	3	**0.454**	**0.035**	*	**0.592**	**0.007**	*
	4	**0.456**	**0.035**	*	**0.477**	**0.029**	*
	5	**0.489**	**0.026**	*	**0.504**	**0.022**	*
KFA	1	**-0.465**	**0.034**	*	-0.317	0.140	
	2	**-0.498**	**0.023**	*	-0.366	0.090	
	3	**-0.515**	**0.019**	*	-0.306	0.150	
	4	**-0.623**	**0.011**	*	-0.380	0.078	
	5	**-0.582**	**0.008**	*	**-0.525**	**0.018**	*

Table 1. Correlations with seizure burden for the PWMB and CB indicate limbic involvement in the progression of cytocarchitectural changes in TLE. ROI numbers correspond to the ROIs depicted in Figure 2, and statistically significant correlations are indicated by bold font and asterisks for $p < 0.05$ after FDR correction for multiple comparisons.

Parahippocampal White Matter Bundle

		Left				Right			
Param	**ROI**	**Control**	**Patient**	**Cohen's d**	**p-value**	**Control**	**Patient**	**Cohen's d**	**p-value**
	1	1.29 (0.24)	1.31 (0.41)	0.037	0.918	1.33 (0.25)	1.41 (0.36)	0.260	0.491
	2	1.19 (0.17)	1.28 (0.27)	0.347	0.343	1.30 (0.18)	1.37 (0.30)	0.261	0.489
MD	3	**1.08 (0.12)**	**1.28 (0.28)**	**0.894**	**0.019**	1.17 (0.16)	1.24 (0.24)	0.347	0.360
	4	1.07 (0.13)	1.27 (0.34)	0.734	0.050	1.08 (0.15)	1.12 (0.20)	0.238	0.529
	5	1.12 (0.19)	1.30 (0.34)	0.655	0.079	1.11 (0.18)	1.10 (0.20)	-0.048	0.898
	1	0.16 (0.03)	0.16 (0.04)	-0.150	0.680	0.16 (0.04)	0.15 (0.04)	-0.228	0.546
	2	0.19 (0.02)	0.18 (0.04)	-0.386	0.292	0.18 (0.04)	0.18 (0.04)	-0.122	0.745
FA	3	0.20 (0.03)	0.18 (0.04)	-0.536	0.147	0.20 (0.04)	0.19 (0.04)	-0.384	0.311
	4	0.17 (0.04)	0.15 (0.04)	-0.539	0.145	0.20 (0.04)	0.18 (0.03)	-0.496	0.194
	5	0.12 (0.04)	0.14 (0.04)	0.337	0.356	0.16 (0.04)	0.15 (0.04)	-0.176	0.641
	1	0.75 (0.04)	0.75 (0.07)	-0.045	0.902	0.77 (0.04)	0.78 (0.08)	0.119	0.752
	2	0.75 (0.06)	0.77 (0.06)	0.190	0.601	0.79 (0.04)	0.80 (0.06)	0.210	0.577
MK	3	0.73 (0.10)	0.76 (0.07)	0.337	0.357	0.78 (0.05)	0.81 (0.05)	0.493	0.196
	4	0.69 (0.09)	0.73 (0.09)	0.446	0.225	0.75 (0.05)	0.79 (0.09)	0.443	0.244
	5	0.67 (0.11)	0.72 (0.08)	0.604	0.104	0.73 (0.06)	0.75 (0.09)	0.253	0.503
	1	0.22 (0.08)	0.23 (0.09)	0.038	0.916	0.21 (0.09)	0.19 (0.10)	-0.233	0.537
	2	0.25 (0.08)	0.23 (0.08)	-0.293	0.421	0.22 (0.07)	0.20 (0.08)	-0.188	0.617
KFA	3	**0.30 (0.08)**	**0.23 (0.09)**	**-0.778**	**0.039**	0.26 (0.07)	0.23 (0.09)	-0.362	0.340
	4	**0.29 (0.09)**	**0.22 (0.10)**	**-0.739**	**0.049**	0.31 (0.09)	0.26 (0.09)	-0.502	0.189
	5	0.24 (0.10)	0.20 (0.08)	-0.525	0.155	0.26 (0.08)	0.26 (0.09)	0.022	0.952

Cingulum Bundle

		Left				Right			
Param	**ROI**	**Control**	**Patient**	**Cohen's d**	**p-value**	**Control**	**Patient**	**Cohen's d**	**p-value**
	1	0.91 (0.06)	0.96 (0.06)	0.724	0.053	0.94 (0.08)	0.95 (0.08)	0.155	0.669
	2	0.88 (0.07)	0.92 (0.08)	0.646	0.083	0.90 (0.08)	0.92 (0.07)	0.296	0.417
MD	3	0.85 (0.06)	0.89 (0.07)	0.629	0.091	0.89 (0.09)	0.90 (0.07)	0.145	0.690
	4	0.85 (0.06)	0.90 (0.09)	0.668	0.073	0.87 (0.09)	0.90 (0.10)	0.329	0.369
	5	**0.84 (0.05)**	**0.89 (0.08)**	**0.773**	**0.040**	0.84 (0.07)	0.90 (0.13)	0.579	0.118
	1	**0.21 (0.05)**	**0.18 (0.04)**	**-0.792**	**0.036**	0.17 (0.04)	0.16 (0.03)	-0.261	0.474
	2	**0.29 (0.06)**	**0.23 (0.07)**	**-1.032**	**0.007**	0.22 (0.05)	0.22 (0.05)	-0.089	0.807
FA	3	**0.36 (0.06)**	**0.29 (0.06)**	**-1.153**	**0.003**	0.27 (0.07)	0.27 (0.07)	-0.047	0.896
	4	**0.35 (0.05)**	**0.31 (0.07)**	**-0.790**	**0.036**	0.30 (0.09)	0.27 (0.06)	-0.445	0.226
	5	**0.31 (0.06)**	**0.26 (0.06)**	**-0.806**	**0.033**	0.28 (0.08)	0.23 (0.06)	-0.628	0.091
	1	0.83 (0.07)	0.85 (0.06)	0.289	0.428	0.81 (0.08)	0.83 (0.07)	0.241	0.507
	2	0.83 (0.09)	0.88 (0.09)	0.511	0.166	0.81 (0.08)	0.87 (0.09)	0.752	0.045
MK	3	0.86 (0.13)	0.91 (0.10)	0.426	0.246	0.83 (0.10)	0.90 (0.10)	0.689	0.065
	4	0.87 (0.10)	0.92 (0.09)	0.502	0.173	0.84 (0.09)	0.89 (0.10)	0.534	0.148
	5	0.86 (0.12)	0.90 (0.09)	0.443	0.228	0.83 (0.10)	0.89 (0.09)	0.631	0.090
	1	**0.45 (0.08)**	**0.37 (0.08)**	**-1.031**	**0.008**	0.38 (0.06)	0.34 (0.08)	-0.551	0.136
	2	**0.57 (0.09)**	**0.45 (0.10)**	**-1.262**	**0.001**	0.49 (0.10)	0.42 (0.10)	-0.594	0.109
KFA	3	**0.63 (0.10)**	**0.53 (0.09)**	**-1.102**	**0.005**	0.53 (0.12)	0.49 (0.10)	-0.433	0.239
	4	**0.59 (0.09)**	**0.49 (0.10)**	**-1.055**	**0.006**	0.52 (0.13)	0.47 (0.11)	-0.437	0.234
	5	**0.50 (0.11)**	**0.40 (0.09)**	**-0.927**	**0.015**	**0.46 (0.12)**	**0.37 (0.11)**	**-0.776**	**0.039**

Table 2. Group-wise comparisons between subjects whose seizures are well-controlled with AEDs (n = 13) and subjects whose seizures are not well-controled by AEDs (n =

19) in PWMB and CB pathways. Differences with $p < 0.05$ (uncorrected) are indicated by bold font. These may be regarded as trends, as no differences where significant after correcting for multiple comparisons.

Online Supplemental Material: Image Acquisition and Data Analysis

Image Acquisition

DKI datasets were acquired with a 3 Tesla Magnetom Verio MRI scanner (Siemens Medical, Erlangen, Germany) using a vendor-supplied, single-shot diffusion-weighted EPI sequence with a twice-refocused spin echo (1) and a 12-channel head coil. To characterize non-Gaussian diffusion, the protocol included 3 diffusion weightings of b = 0, 1000, and 2000 s/mm^2, with 30 isotropically distributed diffusion encoding directions and a total of 10 images with no diffusion weighting (b=0). Other acquisition parameters were: repetition time (TR) = 8500 ms, echo time (TE) = 98 ms, voxel dimensions = 3.0×3.0×3.0 mm^3, matrix size × number of slices = 74×74×40, and a parallel imaging factor = 2 with no partial Fourier encoding. The acquisition time for this protocol was 9 minutes and 12 seconds. Structural imaging was also performed for each participant using a sagittal T1-weighted magnetization-prepared rapid acquisition gradient echo (MPRAGE) image sequence, with TR/TE = 2250/4.18 ms, inversion time = 900 ms, voxel dimensions = 1.0×1.0×1.0 mm^3, and matrix size × number of slices = 256×256×176.

Image Analysis

DKI analysis included the estimation of the diffusion and kurtosis tensors (2) and subsequent DKI-derived tractography (3,4) and was performed using diffusional kurtosis estimator (DKE) software (https://www.nitrc.org/projects/dke/). Quantitative tensor analyses included characterization of mean diffusivity (MD) and FA from the diffusion

tensor and corresponding mean kurtosis (MK) (2) and kurtosis fractional anisotropy (KFA) (5). DKI was incorporated into the AFQ image processing pipeline (https://github.com/jyeatman/AFQ) using fully automated in-house scripts written in MATLAB (MathWorks, Natick, MA, USA).

AFQ utilizes diffusion tractography data and performs a series of automated steps to identify and segment specific WM fiber bundles and isolate the core of each tract (6). Fiber bundles are selected by specifying regions of interest (ROIs) chosen from a WM template, which are applied to define the extremities of each tract. Once the core of a tract is identified, AFQ interpolates a fixed number of sections along the tract and estimates the diffusion and kurtosis tensors at every section, enabling reconstruction of all tensor-derived metrics. By using each subject's unique tractography data, this approach can potentially accommodate more inter-subject variability in tract locations than alternative voxel-based methods. Tract profiles were excluded in cases where AFQ did not identify individual tracts (7).

Beyond the conventional AFQ pipeline, we implemented in-house algorithms to automatically segment the fimbria-fornix (FF) WM fibers, in addition to the standard fiber groups used by AFQ. This was done as hippocampal sclerosis is a common pathological feature of TLE and the FF represents a major conduit of information to and from the hippocampus. Additional WM pathways were selected based on their hypothesized role in TLE, and include the parahippocampal white matter bundle (PWMB), arcuate fasciculus (AF), inferior longitudinal fasciculus (ILF), cingulum bundle (CB) and uncinate fasciculus (UF).

Tractography

DKI tractography was performed using the closed-form analytical expression of the kurtosis orientation distribution function derived by Jensen et al. (3) and the image analysis procedures developed by Glenn et al. (4) using the DKE tractography module (https://www.nitrc.org/projects/dke/). Whole brain masks were calculated within AFQ using FSL's brain extraction tool, and DKI-based tractography was performed using the Euler method with an angle cutoff threshold of 35 degrees, a minimum tract length threshold of 20 mm, and 250,000 seed points randomly placed within each subject's brain mask.

Statistical Analysis

Tract profiles were created for each fiber group using AFQ along 100 sections by interpolating the DKI-derived diffusion and kurtosis tensors along each tract and then quantifying the tensor-derived parameters for each section. Each tract was then divided into 5 regions of interest (ROIs), consisting of 20 consecutive sections. The respective along-the-tract diffusion metrics were averaged over each ROI and a two sample t-test was performed to determine the significance of group-wise differences. In all, there were a total of 12 fiber groups × 4 diffusion metrics × 5 regions of interest per fiber group, resulting in 240 total comparisons. Significance levels were corrected for multiple comparisons using the false discovery rate (FDR) procedure (8). To quantify the effect size of the observed changes, the Cohen's d parameter was calculated for each ROI for

group-wise differences as well as differences between subjects whose seizures were well-controlled with AEDs and those whose seizures were not well-controlled with AEDs. All group comparisons were unblinded.

REFERENCES

1. Reese TG, Heid O, Weisskoff RM, Wedeen VJ (2003): Reduction of eddy-current-induced distortion in diffusion MRI using a twice-refocused spin echo. Magn Reson Med. 49:177-82.
2. Tabesh A, Jensen JH, Ardekani BA, Helpern JA (2011): Estimation of tensors and tensor-derived measures in diffusional kurtosis imaging. Magn Reson Med. 65:823-36.
3. Jensen JH, Helpern JA, Tabesh A (2014): Leading non-Gaussian corrections for diffusion orientation distribution functions. NMR Biomed. 27:202-11.
4. Glenn GR, Helpern JA, Tabesh A, Jensen JH. Optimization of white matter fiber tractography with diffusional kurtosis imaging. NMR Biomed. NMR Biomed. 2015;28:1245-56.
5. Glenn GR, Helpern JA, Tabesh A, Jensen JH (2015c): Quantitative assessment of diffusional kurtosis anisotropy. NMR Biomed. 28:448-59.
6. Yeatman JD, Dougherty RF, Myall NJ, Wandell BA, Feldman HM. Tract profiles of white matter properties: automating fiber-tract quantification. PLoS One. 2012;7:e49790.

7. Johnson RT, Yeatman JD, Wandell BA, Buonocore MH, Amaral DG, Nordahl CW. Diffusion properties of major white matter tracts in young, typically developing children. Neuroimage. 2013;88C:143-154.

8. Benjamini, Yoav; Hochberg, Yosef . Controlling the false discovery rate: a practical and powerful approach to multiple testing. J R Stat Soc Series B. 1995;57:289–300.

Online Supplemental Material: Patient Demographic and Clinical Info

Patient Number	Gender	Age (yr)	Age of Epilepsy Onset (yr)	Durration (yr)	Seizure Frequency (per 6 Mo)	MRI Results	Interictal EEG
1	F	57	52	5	3	Normal	Left temporal IEDs
2	F	57	35	22	24	Left HS	Left temporal IEDs
3	F	63	57	6	1	Normal	Left temporal IEDs
4	M	46	3	43	12	Left HS	Left temporal IEDs
5	M	56	30	26	6	Left HS	Left temporal IEDs
6	F	18	3	15	72	Left HS	Left temporal IEDs
7	F	37	33	4	6	Left HS	Left temporal IEDs
8	F	51	50	1	12	Normal	Left temporal IEDs
9	F	23	17	6	6	Left HS	Left and right temporal IEDs
10	M	22	10	12	0.5	Left HS	Left temporal IEDs
11	F	21	20	1	1	Left HS	Left temporal IEDs
12	M	34	15	19	1	Normal	Left temporal IEDs
13	F	58	55	3	1	Left HS	Left temporal IEDs
14	M	20	20	0	0.2	Left HS	Left and right temporal IEDs
15	F	67	66	1	6	Normal	Left temporal IEDs
16	F	62	62	0	0.2	Left HS	Left temporal IEDs
17	F	57	1	56	2	Left HS	Normal
18	F	18	5	13	3	Left HS	Left temporal IEDs
19	F	37	28	9	2	Left HS	Normal
20	F	20	19	1	1	Left HS	Normal
21	F	57	50	7	6	Left HS	Left and right temporal IEDs
22	F	45	33	12	2	Left HS	Normal
23	M	43	0	43	3	Left HS	Normal
24	F	76	30	46	6	Left HS	Left temporal IEDs
25	M	36	17	19	1	Left HS	Normal
26	M	65	59	6	1	Left HS	Normal
27	F	57	2	55	6	Left HS	Left temporal IEDs
28	M	45	27	18	2	Left HS	Normal
29	F	27	27	0	0.2	Left HS	Normal
30	F	59	42	17	3	Left HS	Left temporal IEDs
31	F	46	35	11	0.5	Left HS	Left temporal IEDs
32	M	40	37	3	0.2	Left HS	Normal

Note: HS, hippocampal sclerosis; EEG, electroencephalography; IED, interictal epileptiform discharges; in cases where left and right IEDs were noted, left IEDs were greater than right IEDs and signs of unilateral left HS were present on MRI

Online Supplemental Material: Tract Profile Summary Statistics

Fimbria-Fornix

		Left					Right			
Param	ROI	Control	Patient	Cohen's d	p-value		Control	Patient	Cohen's d	p-value
MD	1	1.81 (0.34)	1.98 (0.46)	-0.423	0.332		1.99 (0.37)	1.98 (0.52)	0.014	0.976
	2	1.91 (0.34)	2.05 (0.40)	-0.378	0.407		1.97 (0.42)	2.04 (0.45)	-0.174	0.744
	3	1.22 (0.25)	1.37 (0.39)	-0.453	0.283		1.24 (0.22)	1.30 (0.34)	-0.241	0.631
	4	1.27 (0.18)	1.40 (0.31)	-0.504	0.212		1.28 (0.17)	1.30 (0.23)	-0.117	0.832
	5	1.15 (0.18)	1.23 (0.25)	-0.357	0.426		1.29 (0.28)	1.22 (0.24)	0.286	0.565
FA	1	0.20 (0.04)	0.19 (0.05)	0.419	0.338		0.19 (0.04)	0.18 (0.05)	0.115	0.829
	2	0.18 (0.05)	0.16 (0.04)	0.317	0.510		0.17 (0.04)	0.16 (0.04)	0.261	0.589
	3	0.28 (0.07)	0.26 (0.07)	0.268	0.594		0.28 (0.06)	0.25 (0.06)	0.460	0.276
	4	0.24 (0.04)	0.22 (0.05)	0.343	0.448		0.24 (0.05)	0.23 (0.05)	0.268	0.593
	5	0.21 (0.04)	0.19 (0.07)	0.250	0.619		0.20 (0.05)	0.20 (0.05)	0.110	0.822
MK	1	0.71 (0.08)	0.66 (0.09)	0.590	0.116		0.68 (0.08)	0.68 (0.10)	0.068	0.920
	2	0.69 (0.08)	0.65 (0.08)	0.435	0.311		0.68 (0.09)	0.65 (0.09)	0.242	0.630
	3	0.82 (0.06)	0.77 (0.09)	0.695	0.055		0.83 (0.07)	0.79 (0.09)	0.395	0.388
	4	**0.80 (0.06)**	**0.74 (0.07)**	**0.997**	**< 0.005**	**	0.81 (0.05)	0.78 (0.06)	0.514	0.194
	5	**0.79 (0.05)**	**0.72 (0.07)**	**1.220**	**< 0.005**	**	0.78 (0.06)	0.75 (0.09)	0.447	0.281
KFA	1	0.15 (0.04)	0.16 (0.09)	-0.156	0.772		0.14 (0.04)	0.15 (0.06)	-0.255	0.603
	2	0.13 (0.04)	0.13 (0.04)	0.094	0.877		0.14 (0.04)	0.14 (0.05)	0.051	0.930
	3	0.30 (0.10)	0.27 (0.11)	0.236	0.622		0.28 (0.08)	0.26 (0.08)	0.177	0.745
	4	0.25 (0.06)	0.23 (0.07)	0.241	0.628		0.23 (0.06)	0.24 (0.08)	-0.160	0.765
	5	0.25 (0.07)	0.24 (0.08)	0.052	0.932		0.23 (0.08)	0.23 (0.08)	-0.093	0.882

Parahippocampal White Matter Bundle

		Left					Right		
Param	ROI	Control	Patient	Cohen's d	p-value		Control	Patient	Cohen's d
MD	1	1.25 (0.29)	1.30 (0.34)	-0.168	0.753		1.26 (0.28)	1.38 (0.32)	-0.397
	2	1.23 (0.21)	1.24 (0.24)	-0.066	0.922		1.28 (0.20)	1.34 (0.26)	-0.286
	3	1.18 (0.18)	1.20 (0.25)	-0.091	0.872		1.20 (0.16)	1.21 (0.21)	-0.058
	4	1.14 (0.18)	1.19 (0.29)	-0.225	0.633		1.08 (0.13)	1.10 (0.18)	-0.138
	5	1.14 (0.19)	1.23 (0.30)	-0.379	0.400		1.06 (0.15)	1.11 (0.19)	-0.274
FA	1	0.18 (0.05)	0.16 (0.03)	0.484	0.229		0.17 (0.05)	0.15 (0.04)	0.362
	2	0.20 (0.05)	0.18 (0.03)	0.448	0.288		0.18 (0.04)	0.18 (0.04)	0.091
	3	0.20 (0.04)	0.18 (0.03)	0.361	0.420		0.20 (0.04)	0.20 (0.04)	-0.015
	4	0.18 (0.03)	0.16 (0.04)	0.620	0.092		0.19 (0.04)	0.19 (0.04)	0.087
	5	0.15 (0.03)	0.13 (0.04)	0.479	0.234		0.15 (0.03)	0.16 (0.04)	-0.014
MK	1	0.79 (0.06)	0.75 (0.06)	0.659	0.066		0.80 (0.05)	0.77 (0.06)	0.511
	2	**0.80 (0.05)**	**0.76 (0.06)**	**0.810**	**0.018**	*	0.82 (0.04)	0.79 (0.05)	0.608
	3	0.79 (0.05)	0.74 (0.08)	0.668	0.064		0.81 (0.04)	0.80 (0.05)	0.311
	4	0.76 (0.07)	0.72 (0.09)	0.565	0.127		0.76 (0.08)	0.77 (0.08)	-0.196
	5	**0.75 (0.05)**	**0.70 (0.10)**	**0.708**	**0.045**	*	0.74 (0.09)	0.74 (0.08)	-0.040
KFA	1	1.26 (0.28)	1.38 (0.32)	-0.397	0.383		0.21 (0.09)	0.20 (0.09)	0.127
	2	1.28 (0.20)	1.34 (0.26)	-0.286	0.571		0.20 (0.07)	0.21 (0.08)	-0.036
	3	1.20 (0.16)	1.21 (0.21)	-0.058	0.929		0.24 (0.08)	0.24 (0.08)	-0.090
	4	1.08 (0.13)	1.10 (0.18)	-0.138	0.790		0.29 (0.11)	0.28 (0.09)	0.058
	5	1.06 (0.15)	1.11 (0.19)	-0.274	0.589		0.28 (0.10)	0.26 (0.09)	0.200

Note: ROI locations correspond to those illustrated in Figure 2. Control and Patient values represent mean (± sandard deviation). Statistically significant differences are indicated by bold font and with a single asterisk for $p < 0.05$ and a double asterisk for $p < 0.005$, after correcting for multiple comparisons with FDR.

Arcuate Fasciculus

		Left					Right			
Param	**ROI**	**Control**	**Patient**	**Cohen's d**	**p-value**		**Control**	**Patient**	**Cohen's d**	**p-value**
	1	0.80 (0.02)	0.80 (0.05)	-0.111	0.821		0.80 (0.03)	0.80 (0.05)	0.026	0.969
	2	0.82 (0.03)	0.83 (0.05)	-0.237	0.625		0.83 (0.04)	0.83 (0.05)	-0.113	0.826
MD	3	0.84 (0.03)	0.85 (0.06)	-0.279	0.572		0.85 (0.03)	0.86 (0.06)	-0.170	0.750
	4	0.86 (0.03)	0.89 (0.06)	-0.444	0.284		0.88 (0.04)	0.89 (0.07)	-0.320	0.490
	5	0.88 (0.04)	0.89 (0.06)	-0.340	0.445		0.88 (0.04)	0.88 (0.06)	-0.018	0.979
	1	0.36 (0.05)	0.35 (0.06)	0.173	0.746		0.33 (0.06)	0.33 (0.08)	-0.069	0.923
	2	0.34 (0.06)	0.33 (0.05)	0.164	0.752		0.33 (0.07)	0.34 (0.06)	-0.123	0.811
FA	3	0.37 (0.06)	0.36 (0.07)	0.167	0.751		0.38 (0.06)	0.37 (0.05)	0.142	0.793
	4	**0.31 (0.06)**	**0.28 (0.05)**	**0.763**	**0.026**	*	0.29 (0.06)	0.28 (0.05)	0.029	0.961
	5	**0.41 (0.06)**	**0.35 (0.04)**	**1.118**	**< 0.005**	**	0.41 (0.06)	0.40 (0.06)	0.145	0.785
	1	**1.20 (0.06)**	**1.15 (0.08)**	**0.830**	**0.016**	*	1.19 (0.06)	1.14 (0.10)	0.621	0.094
	2	**1.18 (0.06)**	**1.11 (0.08)**	**0.946**	**< 0.005**	**	**1.16 (0.06)**	**1.10 (0.09)**	**0.726**	**0.038**
MK	3	**1.14 (0.05)**	**1.07 (0.08)**	**1.210**	**< 0.005**	**	**1.13 (0.06)**	**1.06 (0.09)**	**0.963**	**< 0.005**
	4	**1.11 (0.05)**	**1.03 (0.08)**	**1.360**	**< 0.005**	**	**1.10 (0.06)**	**1.03 (0.09)**	**0.960**	**< 0.005**
	5	**1.09 (0.05)**	**1.02 (0.09)**	**0.936**	**< 0.005**	**	**1.08 (0.06)**	**1.03 (0.09)**	**0.746**	**0.031**
	1	0.54 (0.04)	0.55 (0.07)	-0.236	0.625		0.52 (0.04)	0.53 (0.08)	-0.263	0.587
	2	0.53 (0.04)	0.54 (0.07)	-0.225	0.641		0.54 (0.04)	0.56 (0.08)	-0.225	0.638
KFA	3	0.53 (0.05)	0.53 (0.08)	0.023	0.971		0.52 (0.05)	0.52 (0.07)	0.001	0.997
	4	0.42 (0.05)	0.39 (0.07)	0.440	0.284		0.37 (0.06)	0.38 (0.07)	-0.162	0.758
	5	0.45 (0.06)	0.42 (0.07)	0.476	0.236		0.42 (0.06)	0.43 (0.09)	-0.180	0.748

Inferior Longitudinal Fasciculus

		Left					Right			
Param	**ROI**	**Control**	**Patient**	**Cohen's d**	**p-value**		**Control**	**Patient**	**Cohen's d**	**p-value**
	1	0.97 (0.10)	1.00 (0.12)	-0.309	0.514		0.96 (0.09)	0.97 (0.13)	-0.112	0.821
	2	0.96 (0.09)	0.98 (0.08)	-0.288	0.569		0.97 (0.08)	0.98 (0.09)	-0.052	0.932
MD	3	0.96 (0.06)	1.00 (0.08)	-0.556	0.135		1.00 (0.07)	0.99 (0.09)	0.164	0.756
	4	0.96 (0.06)	0.99 (0.10)	-0.362	0.422		1.00 (0.07)	0.99 (0.10)	0.180	0.745
	5	0.99 (0.09)	1.04 (0.18)	-0.375	0.409		0.99 (0.11)	0.98 (0.12)	0.044	0.949
	1	0.43 (0.10)	0.42 (0.06)	0.136	0.793		0.40 (0.05)	0.39 (0.05)	0.321	0.494
	2	0.41 (0.08)	0.39 (0.06)	0.287	0.562		0.37 (0.05)	0.37 (0.05)	0.145	0.789
FA	3	0.33 (0.07)	0.31 (0.06)	0.420	0.328		0.29 (0.06)	0.30 (0.05)	-0.176	0.749
	4	0.25 (0.06)	0.24 (0.06)	0.260	0.591		0.23 (0.06)	0.22 (0.05)	0.135	0.787
	5	0.18 (0.07)	0.16 (0.05)	0.370	0.409		0.17 (0.06)	0.16 (0.06)	0.158	0.761
	1	**0.98 (0.08)**	**0.92 (0.09)**	**0.793**	**0.021**	*	**1.00 (0.06)**	**0.92 (0.09)**	**1.091**	**< 0.005**
	2	**0.96 (0.06)**	**0.88 (0.09)**	**0.968**	**< 0.005**	**	**0.96 (0.05)**	**0.90 (0.08)**	**0.902**	**0.007**
MK	3	**0.93 (0.06)**	**0.86 (0.09)**	**0.874**	**0.010**	*	0.90 (0.06)	0.86 (0.06)	0.582	0.116
	4	**0.88 (0.06)**	**0.82 (0.08)**	**0.981**	**< 0.005**	**	**0.87 (0.06)**	**0.82 (0.05)**	**0.812**	**0.018**
	5	**0.83 (0.07)**	**0.76 (0.08)**	**1.002**	**< 0.005**	**	**0.83 (0.05)**	**0.76 (0.11)**	**0.782**	**0.023**
	1	0.41 (0.10)	0.42 (0.08)	-0.070	0.924		0.38 (0.06)	0.41 (0.09)	-0.379	0.405
	2	0.39 (0.08)	0.39 (0.09)	-0.018	0.975		0.34 (0.07)	0.37 (0.09)	-0.341	0.445
KFA	3	0.35 (0.08)	0.34 (0.08)	0.138	0.798		0.28 (0.06)	0.33 (0.09)	-0.663	0.065
	4	0.28 (0.07)	0.29 (0.09)	-0.057	0.925		0.25 (0.05)	0.27 (0.07)	-0.352	0.431
	5	0.22 (0.09)	0.22 (0.09)	0.076	0.907		0.22 (0.08)	0.24 (0.11)	-0.174	0.748

Note: ROI locations correspond to those illustrated in Figure 2. Control and Patient values represent mean (± sandard deviation). Statistically significant differences are indicated by bold font and with a single asterisk for $p < 0.05$ and a double asterisk for $p < 0.005$, after correcting for multiple comparisons with FDR.

Cingulum Bundle

		Left				Right			
Param	ROI	Control	Patient	Cohen's d	p-value	Control	Patient	Cohen's d	p-value
MD	1	0.93 (0.05)	0.94 (0.06)	-0.136	0.797	0.91 (0.05)	0.95 (0.08)	-0.591	0.112
	2	0.89 (0.05)	0.91 (0.08)	-0.303	0.525	0.89 (0.05)	0.91 (0.08)	-0.266	0.589
	3	0.86 (0.04)	0.88 (0.07)	-0.297	0.541	0.88 (0.06)	0.90 (0.08)	-0.205	0.679
	4	0.87 (0.04)	0.88 (0.08)	-0.288	0.564	0.89 (0.06)	0.89 (0.10)	-0.059	0.928
	5	0.85 (0.03)	0.87 (0.07)	-0.354	0.429	0.86 (0.04)	0.88 (0.11)	-0.210	0.668
FA	1	0.20 (0.05)	0.19 (0.05)	0.155	0.770	0.19 (0.04)	0.17 (0.03)	0.648	0.072
	2	0.26 (0.06)	0.26 (0.07)	0.003	0.996	0.23 (0.04)	0.22 (0.05)	0.257	0.595
	3	0.31 (0.05)	0.32 (0.07)	-0.133	0.789	0.27 (0.05)	0.27 (0.07)	-0.040	0.951
	4	0.33 (0.05)	0.33 (0.07)	0.068	0.924	0.27 (0.05)	0.28 (0.07)	-0.191	0.714
	5	0.29 (0.05)	0.28 (0.06)	0.141	0.793	0.24 (0.06)	0.25 (0.07)	-0.136	0.801
MK	1	0.87 (0.06)	0.84 (0.07)	0.374	0.407	**0.87 (0.06)**	**0.82 (0.07)**	**0.696**	**0.050**
	2	0.89 (0.07)	0.86 (0.09)	0.355	0.431	0.88 (0.07)	0.85 (0.09)	0.392	0.383
	3	0.94 (0.06)	0.89 (0.11)	0.588	0.112	0.90 (0.07)	0.87 (0.11)	0.368	0.409
	4	0.94 (0.07)	0.90 (0.10)	0.551	0.139	0.91 (0.06)	0.87 (0.09)	0.518	0.184
	5	0.93 (0.06)	0.88 (0.10)	0.614	0.095	0.90 (0.05)	0.87 (0.10)	0.448	0.284
KFA	1	0.41 (0.07)	0.40 (0.09)	0.152	0.771	0.40 (0.07)	0.36 (0.07)	0.533	0.163
	2	0.51 (0.08)	0.50 (0.11)	0.024	0.970	0.47 (0.07)	0.45 (0.11)	0.234	0.622
	3	0.56 (0.07)	0.57 (0.11)	-0.078	0.904	0.52 (0.08)	0.51 (0.11)	0.115	0.832
	4	0.53 (0.06)	0.53 (0.11)	0.003	0.998	0.47 (0.08)	0.49 (0.12)	-0.181	0.749
	5	0.41 (0.06)	0.44 (0.11)	-0.349	0.430	0.40 (0.08)	0.41 (0.12)	-0.114	0.828

Uncinate Fasciculus

		Left					Right		
Param	ROI	Control	Patient	Cohen's d	p-value		Control	Patient	Cohen's d
MD	1	0.96 (0.08)	0.97 (0.14)	-0.023	0.970		0.93 (0.12)	0.94 (0.10)	-0.135
	2	0.96 (0.16)	0.96 (0.17)	-0.007	0.990		0.95 (0.17)	0.94 (0.10)	0.066
	3	1.03 (0.24)	1.02 (0.19)	0.042	0.945		0.99 (0.22)	0.98 (0.09)	0.068
	4	1.04 (0.23)	1.07 (0.27)	-0.100	0.875		1.01 (0.26)	1.03 (0.13)	-0.067
	5	1.05 (0.18)	1.10 (0.26)	-0.239	0.637		1.03 (0.26)	1.13 (0.28)	-0.366
FA	1	0.25 (0.09)	0.26 (0.08)	-0.039	0.951		0.29 (0.09)	0.27 (0.09)	0.288
	2	0.27 (0.08)	0.27 (0.09)	-0.038	0.946		0.28 (0.08)	0.26 (0.07)	0.236
	3	0.26 (0.09)	0.26 (0.09)	-0.044	0.952		0.28 (0.08)	0.26 (0.08)	0.207
	4	0.25 (0.08)	0.23 (0.08)	0.241	0.635		0.27 (0.08)	0.24 (0.07)	0.430
	5	0.20 (0.07)	0.18 (0.07)	0.302	0.572		0.24 (0.06)	0.20 (0.08)	0.608
MK	1	0.78 (0.05)	0.74 (0.07)	0.622	0.123		0.77 (0.06)	0.75 (0.10)	0.248
	2	0.80 (0.06)	0.76 (0.10)	0.533	0.222		0.78 (0.06)	0.76 (0.09)	0.255
	3	0.80 (0.05)	0.76 (0.09)	0.654	0.109		0.79 (0.08)	0.77 (0.08)	0.278
	4	**0.81 (0.05)**	**0.74 (0.12)**	**0.851**	**0.023**	*	0.80 (0.07)	0.77 (0.09)	0.300
	5	**0.81 (0.05)**	**0.74 (0.10)**	**0.945**	**0.011**	*	0.81 (0.06)	0.78 (0.08)	0.476
KFA	1	0.34 (0.12)	0.36 (0.12)	-0.161	0.784		0.42 (0.13)	0.37 (0.12)	0.404
	2	0.33 (0.12)	0.36 (0.13)	-0.297	0.583		0.35 (0.12)	0.32 (0.10)	0.333
	3	0.26 (0.11)	0.29 (0.11)	-0.274	0.601		0.29 (0.10)	0.29 (0.11)	-0.045
	4	0.26 (0.10)	0.29 (0.13)	-0.259	0.629		0.28 (0.11)	0.27 (0.10)	0.132
	5	0.23 (0.08)	0.25 (0.12)	-0.194	0.747		0.26 (0.09)	0.23 (0.09)	0.339

Note: ROI locations correspond to those illustrated in Figure 2. Control and Patient values represent mean (± sandard deviation). Statistically significant differences are

indicated by bold font and with a single asterisk for $p < 0.05$ and a double asterisk for $p < 0.005$, after correcting for multiple comparisons with FDR.